Flat Bands in Magic-Angle Bilayer Photonic Crystals at Small Twists

Kaichen Dong, Tiancheng Zhang, Jiachen Li, Qingjun Wang, Fuyi Yang, Yoonsoo Rho, Danqing Wang, Costas P. Grigoropoulos, Junqiao Wu, and Jie Yao

Phys. Rev. Lett. **126**, 223601 — Published 2 June 2021
DOI: 10.1103/PhysRevLett.126.223601

Flat bands in magic-angle bilayer photonic crystals at small twists

Kaichen Dong[1,2 †], Tiancheng Zhang[1,3 †], Jiachen Li[1,2], Qingjun Wang[1], Fuyi Yang[1], Yoonsoo Rho[4], Danqing Wang[1,2], Costas P. Grigoropoulos[4], Junqiao Wu[1,2], and Jie Yao[1,2 *]

[1]Department of Materials Science and Engineering, University of California, Berkeley, CA, 94720, USA.

[2]Division of Materials Sciences, Lawrence Berkeley National Laboratory, Berkeley, CA, 94720, USA.

[3]School of Electronics Engineering and Computer Science, Peking University, Beijing 100871, P. R. China.

[4]Department of Mechanical Engineering, University of California, Berkeley, CA, 94720, USA.

* Correspondence to: yaojie@berkeley.edu

† These authors contributed equally to the work

The new physics of magic-angle twisted bilayer graphene (TBG) motivated extensive studies of flat bands hosted by moiré superlattices in van der Waals structures, inspiring the investigations into their photonic counterparts with potential applications including Bose–Einstein condensation. However, correlation between photonic flat bands and bilayer photonic moiré systems remains unexplored, impeding further development of

moiré photonics. In this work, we formulate a coupled-mode theory for low-angle twisted bilayer honeycomb photonic crystals as a close analogy of TBG, discovering magic-angle photonic flat bands with a non-Anderson-type localization. Moreover, the interlayer separation constitutes a convenient degree of freedom in tuning photonic moiré bands without high pressure. A phase diagram is constructed to correlate the twist angle and separation dependencies to the photonic magic angles. Our findings reveal a salient correspondence between fermionic and bosonic moiré systems and pave the avenue toward novel applications through advanced photonic band/state engineering.

Moiré superlattices formed in twisted bilayer van der Waals structures have been widely investigated with exotic phenomena discovered [1-7], including fractional Chern insulators [8], moiré excitons [9], topological physics [10], and band engineering at high pressures [11]. Considering various moiré systems demonstrated so far, the TBG system is the most representative with the feature of a mini-Brillouin zone arising from moiré superlattices [1-3,12-14]. The report of interlayer hybridization induced magic-angle effects in TBG is among the milestones of moiré physics, especially the flat momentum-space dispersion characteristics with nearly zero Fermi velocities and singularities in its density of states [1-3,15]. Along with the surge of research into magic-angle moiré bilayers in condensed matter physics, photonic moiré superlattices are also quickly gaining interests, with demonstrations of Anderson localization and optical solitons in quasi-crystals using monolayer moiré patterns in three-dimensional photorefractive materials at large twist angles [16-18]. Even though the unique correspondence between condensed matter systems and photonic systems has promised moiré photonics with potential breakthroughs [12,16,18,19], a quantitative analysis of the photonic analogy of magic-angle moiré systems is still lacking: the existence of small magic angles in moiré photonic systems has not been observed and more importantly, a complete model to characterize low-angle twisted photonic bilayers would guide the exploration and application of twisted photonic systems.

In this work, we report a theoretical model of low-angle twisted bilayer photonic crystals (TBPC) to solve the photonic moiré bands. By stacking two layers of two-dimensional photonic crystals with a small twist angle and a subwavelength interlayer separation, photonic magic angles are discovered with signatures of photonic flat bands, zero light group velocities and spiky photonic density of states. A modified tight binding model is developed to take into account high coupling orders in the reciprocal space and optical losses, followed by the formulation of a continuum description for optical modes. Using this model, a phase diagram of photonic magic-angle effects as a function of the twist angle and the interlayer separation is established and found to be consistent with full-wave simulations. The remarkable design flexibility of electromagnetic response from the photonic systems makes TBPC an exceptional platform toward better understandings of moiré physics in general, including new configurations that are not easily achievable in electronic systems.

Figure 1(a) shows schematically the configuration of TBPC considered in this work. We start with a model system based on two identical honeycomb arrays of silicon nano-disks working at telecommunication wavelengths, which are photonic counterparts of graphene. Our theoretical model for TBPC (Fig. 1(b)) begins with a well-defined transverse electric (TE) mode hosted in a single disk unit, and we use the coupled mode theory to quantify the coupling between NN disks. Next, in the same spirit of TBG theory [1], the local and periodic interlayer coupling in TBPC allows the use of a continuum model for photonic moiré band calculations. As shown later, specific combinations of the twist angle and the interlayer separation [20] could lead to photonic magic-angle effects in TBPC.

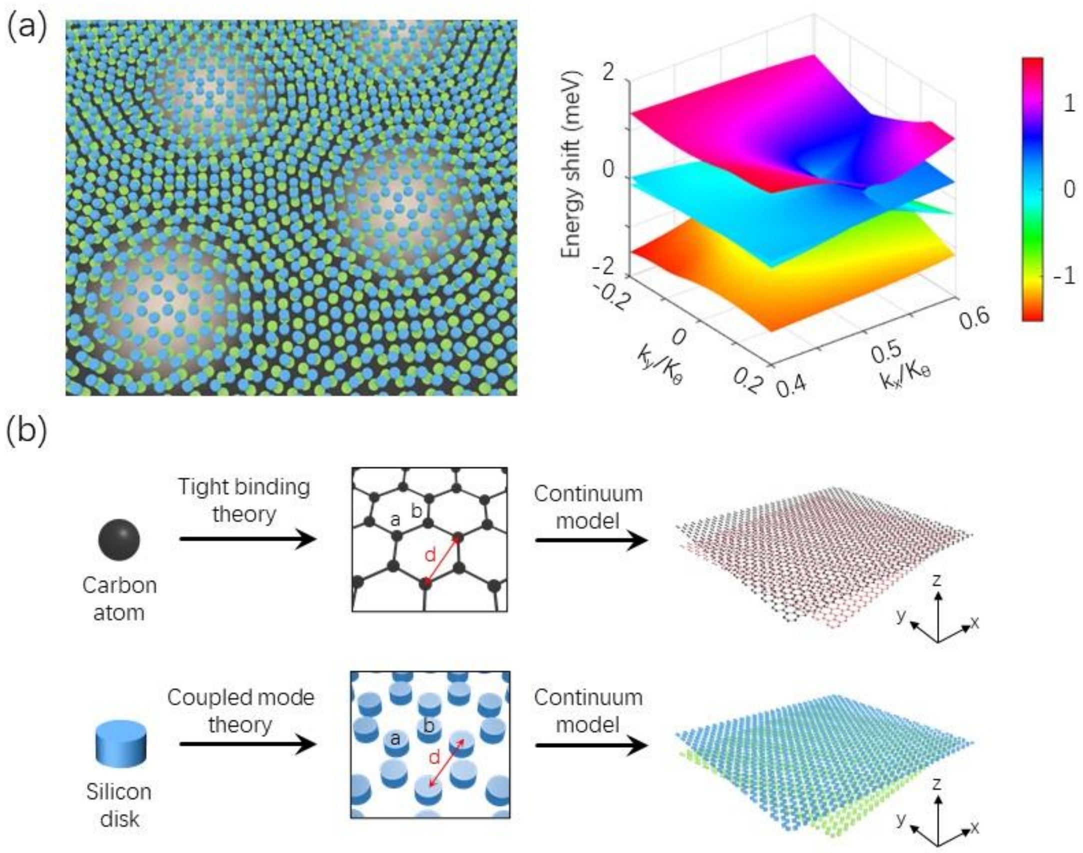

FIG. 1. The TBPC system. (a) Schematic of TBPC with light localized in the AA stacking regions when a photonic magic angle is present (left), along with one representative

dispersion of flat moiré bands leading to such localized modes (right). The lattice constant of monolayer honeycomb photonic crystal is 1.2 μm, while each nano-disk is 220 nm high with a diameter of 400 nm. The moiré bands are analytically calculated with a twist angle and interlayer separation of 5.09° and 50 nm, respectively. Note that the band flattening effect occurs in the 2nd and 3rd bands, which are around the 0 meV energy shift. (b) Comparison between the theoretical models for TBG and TBPC. Similar to TBG, the disks in TBPC fall into two categories: disk 'a' and disk 'b'. However, the coupled modes in TBPC are subject to non-negligible optical losses. The lattice constants for graphene and honeycomb photonic crystal are both denoted as 'd' [31, 32]. The reference frame is also illustrated where z-axis is perpendicular to photonic crystal planes.

We consider two coupled disks of the same shape and material. When the two disks (disk 1 and disk 2) are placed closely enough, the crosstalk between different cavity modes occurs, which is described by the coupled-mode theory [33, 34]:

$$\begin{cases} \frac{da_1}{dt} = (i\omega_1 - \kappa_1)a_1 + ig_{12}a_2 \\ \frac{da_2}{dt} = (i\omega_2 - \kappa_2)a_2 + ig_{21}a_1 \end{cases} \tag{1}$$

where i, a, κ and ω are the imaginary unit, the mode intensity, the decay rate and the angular frequency, respectively. Note that $\kappa_1 = \kappa_2 = \kappa_0$ and $\omega_1 = \omega_2 = \omega_0$ for identical disks. Without loss of generality, we set $g_{12} = g_{21} = g$ [20].

For a monolayer honeycomb disk array with a lattice constant a_0, two subsets of disks exist and are denoted as 'a' and 'b' [32, 35]. The NN of one 'a' disk is three 'b' disks and vice versa. Thus, the equations of each disk could be written as:

$$\begin{cases} \frac{da_j}{dt} = (i\omega_0 - \kappa_0)a_j + \sum_{\boldsymbol{\delta}}\left(igb_{j+\boldsymbol{\delta}}\right) \\ \frac{db_j}{dt} = (i\omega_0 - \kappa_0)b_j + \sum_{\boldsymbol{\delta}'}\left(iga_{j+\boldsymbol{\delta}'}\right) \end{cases} \tag{2}$$

where $\boldsymbol{\delta}$ and $\boldsymbol{\delta}'$ are the site-to-site displacement with respect to disk 'a_j' and 'b_j', respectively [20]. Note that j is the serial number for different disks.

Using $a_j = \frac{1}{\sqrt{N}}\sum_{\boldsymbol{k}} \exp\left(-i\boldsymbol{k}\cdot\boldsymbol{r}_{j,a}\right) a_{\boldsymbol{k}}$ and $b_j = \frac{1}{\sqrt{N}}\sum_{\boldsymbol{k}} \exp\left(-i\boldsymbol{k}\cdot\boldsymbol{r}_{j,b}\right) b_{\boldsymbol{k}}$ [36], where $\boldsymbol{r}_{j,a}$ ($\boldsymbol{r}_{j,b}$) is the vector position of a_j (b_j) and N is the total number of 'a' (or 'b') disks, Fourier transform is conducted and Eq. (2) is transformed into:

$$\begin{cases} \frac{da_{\boldsymbol{k}}}{dt} = (i\omega_0 - \kappa_0)a_{\boldsymbol{k}} + igb_{\boldsymbol{k}}\sum_{\boldsymbol{\delta}} \exp(-i\boldsymbol{k}\cdot\boldsymbol{\delta}) \\ \frac{db_{\boldsymbol{k}}}{dt} = (i\omega_0 - \kappa_0)b_{\boldsymbol{k}} + iga_{\boldsymbol{k}}\sum_{\boldsymbol{\delta}'} \exp(-i\boldsymbol{k}\cdot\boldsymbol{\delta}') \end{cases} \tag{3}$$

Now in the reciprocal space, we can see from the equations that the modes localized in 'a' sites ('a' modes for brevity) with wavevector $\boldsymbol{k}$ will only couple to the 'b' modes with wavevector $\boldsymbol{k}$. This is due to the phase-match mechanism [20]. The formation of Dirac cones is detailed in [20].

In the following, we consider the TBPC case where two identical honeycomb photonic crystal layers are stacked with a small twist angle. When the twist angle is commensurate, the superlattice is strictly periodic and the lattice constant is approximately a_0/θ. The mini Brillouin zone of the superlattice is constructed from the difference between the two $\boldsymbol{K}$ wavevectors at the K point for the two layers (denoted as $\boldsymbol{K}_1$ and $\boldsymbol{K}_2$), as shown in Fig. 2(a).

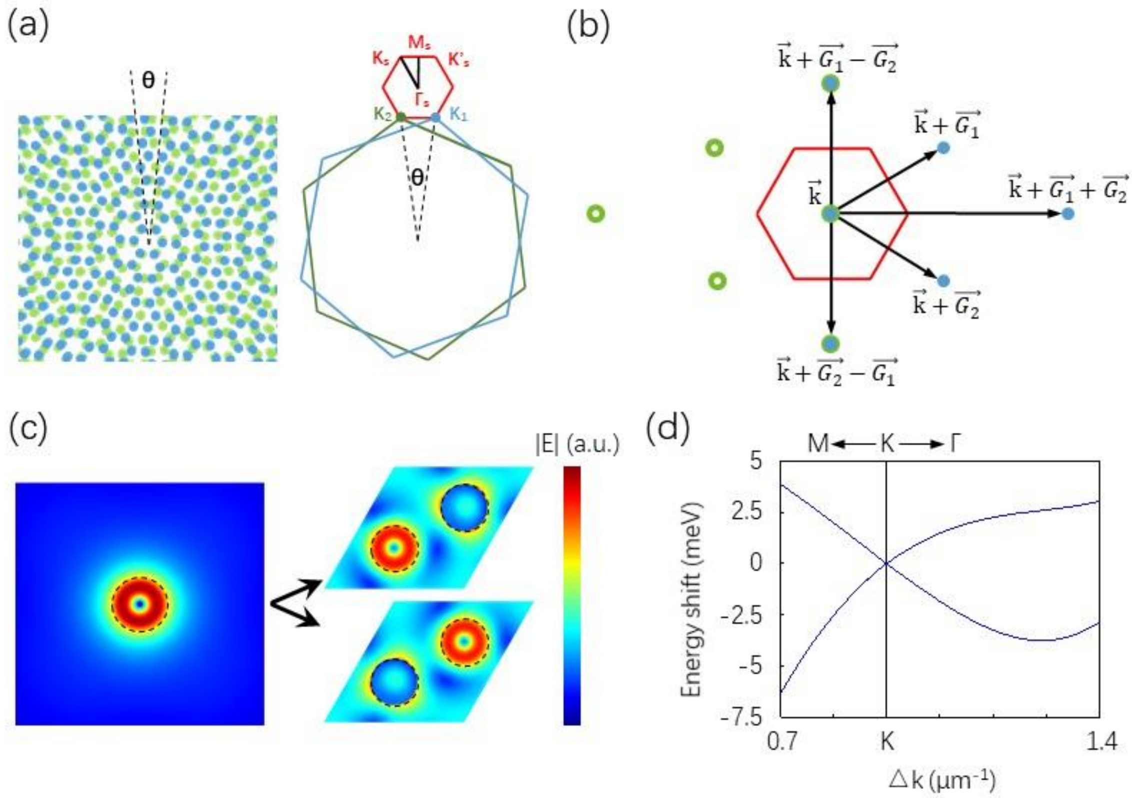

FIG. 2. Inter-site coupling features in TBPC. (a) Top-view of TBPC in the real space showing moiré patterns due to a twist (left) and the mini Brillouin zone hosted by the moiré superlattices (right). (b) TBPC inter-site coupling in the reciprocal space, where blue solid dots and green circles stand for the different modes with specific wavevectors in the photonic crystal layer #1 and layer #2, respectively. The red hexagon denotes the mini Brillouin zone. (c) The numerically solved TE mode in a nano-disk (left) and the double-degenerated states at the Dirac point in a monolayer honeycomb photonic crystal. The disk positions are indicated by dashed circles. The |E| fields are normalized separately in each panel. (d) The corresponding Dirac-point feature in the photonic band structure along the M-K-Γ direction.

Since both photonic crystal layers can be characterized by Eq. (1-3), we now have four sets of disks: a_1, b_1, a_2, and b_2, which represent 'a' and 'b' disks in layer #1 and layer #2, respectively. Here, we take the disk a_{1j} as an example. By only considering NN sites for interlayer coupling, we have:

$$\frac{da_{1j}}{dt} = (i\omega_0 - \kappa_0)a_{1j} + \sum_{\boldsymbol{\delta_1}}\left(ig_{intra}b_{1(j+\delta_1)}\right) + ig(\boldsymbol{l}_{aa})a_{2(j+l_{aa})} + ig(\boldsymbol{l}_{ab})b_{2(j+l_{ab})} \quad (4)$$

where $\boldsymbol{l}_{aa}$ and $\boldsymbol{l}_{ab}$ mean the displacement from disk a_{1j} to its closest 'a' disk and 'b' disk in layer #2, respectively. Note that for the interlayer crosstalk, we consider the coupling only between closest disks. This approximation is generally used in TBG and proved by multiple experiments to be sufficiently accurate [1-3]. The interlayer coupling strength between different sets of disks is given by the function of g, written as $g(\boldsymbol{l}_{aa})$ and $g(\boldsymbol{l}_{ab})$. The function g only depends on the displacement between the two disks in different layers.

Analogous to the monolayer case, we can define $a_{1\boldsymbol{k_1}}, b_{1\boldsymbol{k_1}}, a_{2\boldsymbol{k_2}}$, and $b_{2\boldsymbol{k_2}}$ from: $a_{1j} = \frac{1}{\sqrt{N}}\sum_{\boldsymbol{k}_1}\exp(-i\boldsymbol{k}_1\cdot\boldsymbol{r}_{1j,a})a_{1\boldsymbol{k_1}}$, $b_{1j} = \frac{1}{\sqrt{N}}\sum_{\boldsymbol{k}_1}\exp(-i\boldsymbol{k}_1\cdot\boldsymbol{r}_{1j,b})b_{1\boldsymbol{k}_1}$, $a_{2j} = \frac{1}{\sqrt{N}}\sum_{\boldsymbol{k}_2}\exp(-i\boldsymbol{k}_2\cdot\boldsymbol{r}_{2j,a})a_{2\boldsymbol{k}_2}$, $b_{2j} = \frac{1}{\sqrt{N}}\sum_{\boldsymbol{k}_2}\exp(-i\boldsymbol{k}_2\cdot\boldsymbol{r}_{2j,b})b_{2\boldsymbol{k}_2}$, and apply these equations in Eq. (4) for the Fourier transform:

$$\frac{da_{1k_1}}{dt} = (i\omega_0 - \kappa_0)a_{1\boldsymbol{k}_1} + ig_{intra}b_{1\boldsymbol{k}_1}\sum_{\boldsymbol{\delta_1}}(-i\boldsymbol{k}_1\cdot\boldsymbol{\delta}_1) + \sum_{\boldsymbol{k}_2}\left(\zeta_{aa}(\boldsymbol{k}_1,\boldsymbol{k}_2)a_{2\boldsymbol{k}_2} + \zeta_{ab}(\boldsymbol{k}_1,\boldsymbol{k}_2)b_{2\boldsymbol{k}_2}\right) \quad (5)$$

where $\zeta_{aa}(\boldsymbol{k}_1,\boldsymbol{k}_2)$ (or $\zeta_{ab}(\boldsymbol{k}_1,\boldsymbol{k}_2)$) are the coupling strength between $a_{1\boldsymbol{k}_1}$ and $a_{2\boldsymbol{k}_2}$ (or $b_{2\boldsymbol{k}_2}$). Here, we define the unit area of superlattice as S_c. Using the continuum model, $\zeta_{aa}(\boldsymbol{k}_1,\boldsymbol{k}_2)$ can be written as:

$$\zeta_{aa}(\boldsymbol{k}_1,\boldsymbol{k}_2)=\frac{i}{S_c}\int \exp(i(\boldsymbol{k}_1-\boldsymbol{k}_2)\cdot\boldsymbol{r}_{1,a})\cdot\exp(-i\boldsymbol{k}_2\cdot\boldsymbol{l}_{aa})\cdot g(\boldsymbol{l}_{aa})d^2r_{1,a} \tag{6}$$

After the Fourier transform, the following discussion is in the reciprocal space. Compared to Eq. (3), the first term on the right-hand side of Eq. (5) corresponds to the property of the disk itself, the second term corresponds to the intralayer coupling mechanism, and the last two terms describe the interlayer coupling strength. Due the periodicity of the superlattice, the factor $\exp(-i\boldsymbol{k}_2\cdot\boldsymbol{l}_{aa})\cdot g(\boldsymbol{l}_{aa})$ is also periodic. Thus ζ is zero almost everywhere except the cases when $\boldsymbol{k}_2-\boldsymbol{k}_1=n\cdot\boldsymbol{G}_1+m\cdot\boldsymbol{G}_2$. Here $\boldsymbol{G}_1$ and $\boldsymbol{G}_2$ are the reciprocal eigenvectors of the superlattice (Fig. 2(b)) [20], which describe the new phase-match mechanism.

Next, the AA point (the center of AA stacking region where the top and bottom honeycomb photonic crystal layers are well aligned [37, 38]) is selected as the origin of coordinates, based on which proper superlattices are chosen. Within the hexagonal superlattice around the AA point, we find $\boldsymbol{l}_{aa}=\boldsymbol{\theta}\times\boldsymbol{r}_{1j,a}$ and $\boldsymbol{K}_0\cdot\boldsymbol{l}_{aa}=-(\boldsymbol{\theta}\times\boldsymbol{K}_0)\cdot\boldsymbol{r}_{1j,a}$, where $\boldsymbol{K}_0$ represents the wavevector of the midpoint between the two K points (one for layer #1 and the other one for layer #2). So, Eq. (6) can be written as [20]:

$$\zeta_{aa}(\boldsymbol{k}_1,\boldsymbol{k}_2)=\frac{i}{S_c}\int \exp\left(i\big(\boldsymbol{k}_1-\boldsymbol{k}_2-(\boldsymbol{\theta}\times\boldsymbol{K}_0)\big)\cdot\boldsymbol{r}_{1,a}\right)\cdot g(\boldsymbol{\theta}\times\boldsymbol{r}_1)d^2r_{1,a} \tag{7}$$

From Eq. (7), we obtain the actual value for the interlayer coupling strength. The NN coupling in real space is a series of inter-wavevector coupling in the reciprocal space. For instance, if we analyze the $\boldsymbol{k}_1=\boldsymbol{k}$ mode in layer #1, the a-a interlayer coupling strength will reach the maximum when $\boldsymbol{k}_2=\boldsymbol{k}$, $\boldsymbol{k}+\boldsymbol{G}_1$, or $\boldsymbol{k}+\boldsymbol{G}_2$, and this maximum coupling strength is denoted as t_1. The second maximum coupling strength t_2 can be found at the following points: $\boldsymbol{k}_2 = \boldsymbol{k} + \boldsymbol{G}_1 - \boldsymbol{G}_2$, $\boldsymbol{k} - \boldsymbol{G}_1 + \boldsymbol{G}_2$, or $\boldsymbol{k} + \boldsymbol{G}_1 + \boldsymbol{G}_2$. Higher orders of t are localized at outer wavevector points. Compared with TBG [1], for the TBPC characterized in this work, the interlayer gap (≤200 nm) is much smaller than the monolayer lattice constant (1.2 μm), so higher orders of coupling are relatively strong and t_2 must be included in the theoretic model. With t_1 and t_2, we are already able to obtain all primary conclusions.

As a result of considering t_1 and t_2, the $\boldsymbol{k}_2 = \boldsymbol{k}$ mode in layer #2 couples to six modes in layer #1 (Fig. 2(b)): $\boldsymbol{k}$, $\boldsymbol{k} + \boldsymbol{G}_1$, $\boldsymbol{k} + \boldsymbol{G}_2$, $\boldsymbol{k} + \boldsymbol{G}_1 - \boldsymbol{G}_2$, $\boldsymbol{k} - \boldsymbol{G}_1 + \boldsymbol{G}_2$, and $\boldsymbol{k} + \boldsymbol{G}_1 + \boldsymbol{G}_2$, and vice versa. Since we have four sets of disks in the TBPC (a_1, b_1, a_2, b_2), a total number of 24 modes are considered in our calculation. We truncated the equation to include these 24 modes (12 for layer #1 and 12 for layer #2), yielding a 24×24 matrix for diagonalization. From this matrix, together with the electric-field distribution of the single-disk TE mode (Fig. 2(c)) that leads to the Dirac cone (Fig. 2(d)) [20], we can obtain the photonic band structures in TBPC with different twist angles and interlayer separation.

Akin to TBG, the photonic moiré bands in TBPC strongly rely on both the twist angle and the interlayer separation. In Fig. 3(a)-3(d), we solve for the photonic band structures of TBPC with different twists and an interlayer separation of 80 nm. Note that we only consider the K point here and the K' point is not shown for simplicity [1,39]. When the twist angle is decreased to 4.6°, the group velocity at the Dirac-point energy partially vanishes, and the hybridized photonic bands get flattened with dispersionless characteristics roughly from M_s

through K_s, corresponding to a photonic magic angle. The density of states is also peaked due to the existence of photonic flat bands. As the twist keeps decreasing, the second photonic magic angle is reached at 3.6°, along with the appearance of magic-angle effects near Γ_s. Further reducing the interlayer twist angle destroys the photonic magic-angle effect. In TBPC, the number of bands in a fixed energy range goes up monotonically with a decreasing twist angle. Here, we evaluate the local bandwidth between the two bands closest to the Dirac-point energy [20], and plot it as a function of the twist angle in Fig. 3(e), which illustrates the evolution of bandwidth narrowing around these two photonic magic angles.

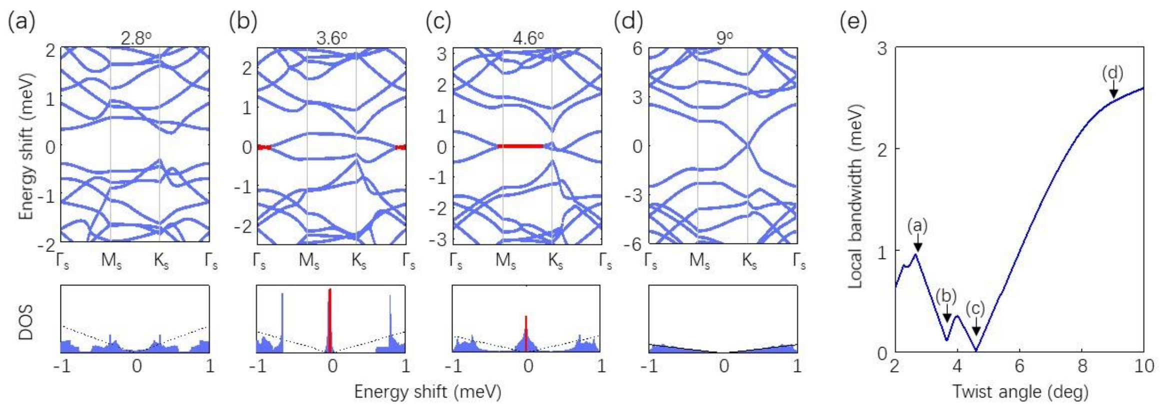

FIG. 3. Photonic moiré band structures. (a-d) Energy dispersions and density of states (DOS) for an interlayer separation of 80 nm and twist angles of 2.8°, 3.6°, 4.6°, and 9°, respectively. The energy is referenced to the Dirac-point energy. Note that when the twist angle equals 3.6° and 4.6°, photonic flat bands appear and are highlighted in red. (e) Local bandwidth of the two photonic bands closest to the Dirac-point energy as functions of the twist angle with an interlayer separation of 80 nm. The bandwidth reaches minimum at the photonic magic angles (3.6° and 4.6°).

Using the above model, we also observe that the photonic magic angles have a strong dependence on the interlayer separation. To quantify the evolution of magic angles with different separation, we normalize the local bandwidth by twist angles [20] and plot it as a function of the twist angle and the interlayer separation in Fig. 4(a). Only low twists are calculated due to local coupling approximation in our theoretical model. Here, the minimal (nearly zero) bandwidths are the direct results of photonic flat bands, and thus are the indicator for photonic magic angles. Two magic-angle traces can be resolved in Fig. 4(a). One notable feature of the photonic magic angle is that smaller interlayer separation leads to larger magic angles: at larger twists, there is a long distance between monolayer Dirac cones, so an enhanced interlayer coupling strength (i.e. a smaller interlayer separation) is required for band flattening by compression. Such a trend in TBPC is in good agreement with pressure-tuned magic angle and band engineering in TBG [40-42]. This correspondence again testifies the uniqueness of TBPC as a fast and versatile platform for understanding and designing moiré superlattice systems with van der Waals bilayers. The influence of t_2 is discussed in [20].

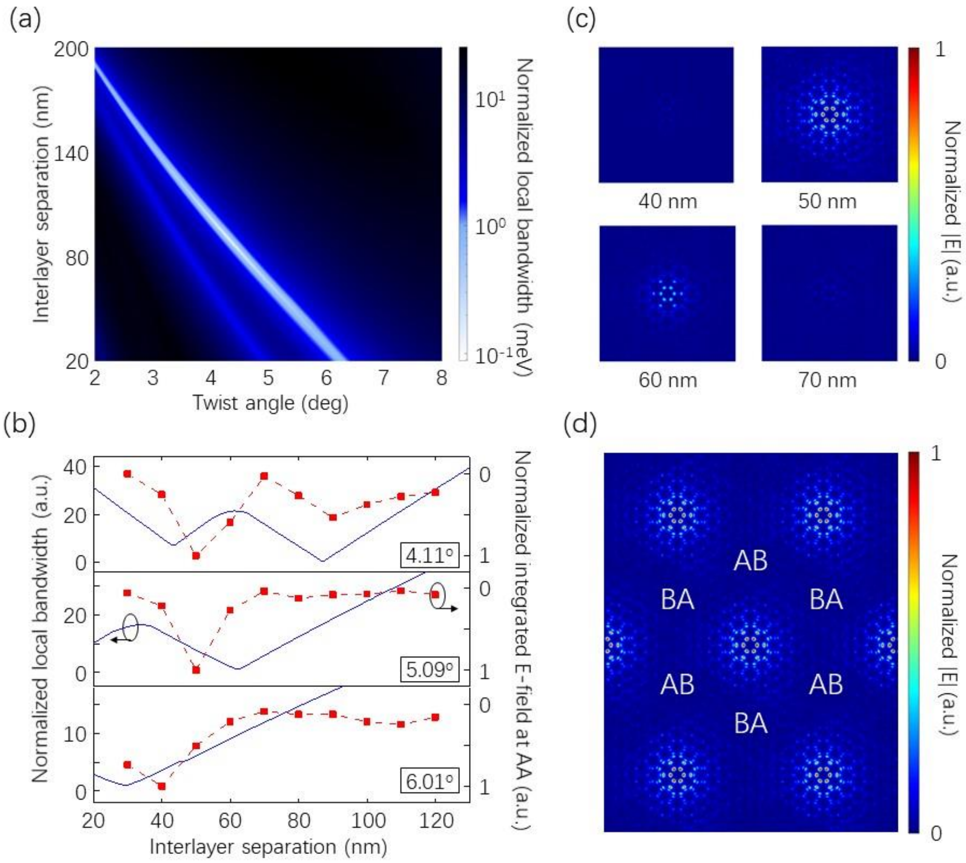

FIG. 4. Phase diagram of photonic magic angles. (a) The phase diagram showing the normalized local bandwidth with varying twist angles and interlayer separation. (b) Comparison between the local bandwidth, and the integrated |E| in the AA region calculated by numerical simulation, which are normalized by the minimum local bandwidth and the maximum integrated |E|, respectively. The dashed line is a guide to the eye. (c) Evolution of |E| profile in the AA region with different interlayer separation and a twist angle of 5.09°. (d) Numerically calculated real-space |E| profile when the twist angle and interlayer separation are 5.09° and 50 nm, respectively.

To test the results of our TBPC model, we perform full-wave numerical simulation of the TBPC with commensurate twist angles of 4.41°, 5.09°, and 6.01° [20], where the moiré superlattice has a rigorous periodicity and can be modeled numerically. Simulation details with additional results can be found in [20]. We find that the photonic flat bands at magic angles lead to a highly localized optical mode in the AA regions, just as the case of TBG. Fig. 4(b) shows good agreement between our theoretical modeling and numerical simulation: wherever the theory predicts the existence of photonic flat bands, a strong peak of numerical |E| in the AA regions can be found nearby. The slight discrepancy here could be reduced by involving higher orders of coupling in the theoretical model (t_3, t_4, etc.).

To further explore the magic-angle effects, the evolution of |E| in the AA region is plotted in Fig. 4(c), showing that the localized mode immediately decays as the interlayer separation deviates from the optimal value for the flat bands. A representative large-area |E| profile associated with photonic flat bands is illustrated in Fig. 4(d), demonstrating strong field localization in AA regions at the magic angles, in contrast to the field localization in large-twist-angle quasi-crystals due to Anderson modes [16,18]. The corresponding H-field profiles also have strong localization in AA regions [20]. Those magic-angle photonic 'hot spots' with zero group velocity may find potential applications in areas such as photoluminescence enhancement [43], molecular vibration detection [44], and slow light generation [45].

In summary, we have discovered the existence of photonic flat bands in two closely coupled planar photonic crystals at certain magic angles. Furthermore, we have formulated a theoretical model to describe the coupling mechanism and calculate the photonic band structure in the twisted bilayer photonic crystals (TBPC). The evolution of photonic magic angle with the interlayer separation reveals a striking similarity between the TBPC and the electronic twisted bilayer graphene (TBG). Extensive numerical simulations further resolve the photonic 'hot spots' localized in the AA regions at the magic angles. Potential experimental realizations include nano-fabrication technologies [46], two-photon polymerization lithography [47], and microwave/acoustic devices [48, 49]. For other bilayer van der Waals moiré structures where moiré band flattening phenomena exist, it is possible that the corresponding TBPC would also host similar photonic behavior if their mathematical descriptions match [20]. Note that a judicious design of the TBPC system is necessary to ensure that the symmetry and coupling conditions of the corresponding van der Waals bilayers are well preserved in TBPC. It is an important future topic to explore approaches that are capable of quantitatively interpreting both the moiré photonics and moiré van der Waals systems. Our model demonstrates an interesting parity between fermionic and bosonic moiré systems, which not only paves the way to the development of moiré photonics, but also serves as a tunable platform for probing and predicting new physics in moiré superlattices generally and in turn guides the exploration of van der Waals structures.

Acknowledgements

This work is funded by the National Science Foundation (NSF) CAREER grant no.

1555336. F.Y. and J.Y. acknowledge support from the U.S. Department of Energy, Office of Science, Office of Basic Energy Sciences, Materials Sciences and Engineering Division under contract DE-AC02-05-CH11231 (Organic-Inorganic Nanocomposites KC3104). This work is partly supported by the U.S. NSF Grant No. ECCS-1953803. We thank Y. Lv and Dr. H. Liu for helpful discussions.

References

1 R. Bistritzer and A. H. MacDonald, Proc. Natl Acad. Sci. USA **108**, 30 (2011).

2 Y. Cao, V. Fatemi, S. Fang, K. Watanabe, T. Taniguchi, E. Kaxiras, and P. Jarillo-Herrero. Nature **556**, 7699 (2018).

3 Y. Cao, V. Fatemi, A. Demir, et al. Nature **556**, 7699 (2018).

4 J. M. B. Lopes Dos Santos, N. M. R. Peres, and A. H. Castro Neto, Phys. Rev. Lett. **99**, 256802 (2007).

5 I. Brihuega, P. Mallet, H. González-Herrero, G. Trambly de Laissardière, M. M. Ugeda, L. Magaud, J. M. Gómez-Rodríguez, F. Ynduráin, and J.-Y. Veuillen. Phys. Rev. Lett. **109**, 196802 (2012).

6 K. Kim, A. DaSilva, S. Huang, B. Fallahazad, S. Larentis, T. Taniguchi, K. Watanabe, B. J. LeRoy, A. H. MacDonald, and E. Tutuc. Proc. Natl Acad. Sci. USA **114**, 13 (2017).

7 Z. Song, Z. Wang, W. Shi, G. Li, C. Fang, and B. A. Bernevig. Phys. Rev. Lett. **123**, 036401 (2019).

8 A. Abouelkomsan, Z. Liu, and E. J. Bergholtz, Phys. Rev. Lett. **124**, 106803 (2020).

9 K. Tran, et al. Nature **567**, 7746 (2019).

10 Q. Tong, H. Yu, Q. Zhu, Y. Wang, X. Xu, and W. Yao. Nat. Phys. **13**, 356 (2017).

11 Y. Gao, X. Lin, T. Smart, P. Ci, K. Watanabe, T. Taniguchi, R. Jeanloz, J. Ni, and Junqiao Wu. Phys. Rev. Lett. **125**, 226403 (2020).

12 S. S. Sunku, et al. Science **362**, 6419 (2018).

13 N. Bultinck, S. Chatterjee, and M. P. Zaletel, Phys. Rev. Lett. **124**, 166601 (2020).

14 G. Tarnopolsky, A. J. Kruchkov, A. Vishwanath, Phys. Rev. Lett. **122**, 106405 (2019).

15 Y. Shimazaki, I. Schwartz, K. Watanabe, T. Taniguchi, M. Kroner, and A. Imamoğlu. Nature **580**, 7804 (2020).

16 P. Wang, Y. Zheng, X. Chen, C. Huang, Y. V. Kartashov, L. Torner, V. V. Konotop, and F. Ye. Nature **577**, 7788 (2020).

17 S.-Y. Jeon, H. Kwon, and K. Hur, Nat. Phys. **13**, 363 (2017).

18 Q. Fu, P. Wang, C. Huang, Y. V. Kartashov, L. Torner, V. V. Konotop, and F. Ye. Nat. Photon. **14**, 663 (2020).

19 Z. Wu and Y. Zheng, Adv. Opt. Mater. **5**, 16 (2017).

20 See Supplemental Materials for theoretical and numerical details and supporting results, which includes Ref. [4, 21-30, 33, 34, 39].

21 N. Leconte, J. Jung, S. Lebègue, and T. Gould. Phys. Rev. B **96**, 195431 (2017).

22 J. van de Groep, T. Coenen, S. A. Mann, and A. Polman. Optica **3**, 1 (2016).

23 M. A. van de Haar, J. van de Groep, B. J.M. Brenny, and A. Polman. Opt. Express **24**, 3 (2016).

24 A. A. Bogdanov, K. L. Koshelev, P. V. Kapitanova, M. V. Rybin, S. A. Gladyshev, Z. F. Sadrieva, K. B. Samusev, Y. S. Kivshar, and M. F. Limonov. Adv. Photon. **1**, 1 (2019).

25 D. Marcuse. IEEE J. Quantum Electron. **21**, 11 (1985).

26 W. Suh, Z. Wang, and S. Fan. IEEE J. Quantum Electron. **40**, 10 (2004).

27 J. M. B. Lopes dos Santos, N. M. R. Peres, and A. H. Castro Neto. Phys. Rev. B. **86**, 155449 (2012)

28 L. Zou, H. C. Po, A. Vishwanath, and T. Senthil. Phys. Rev. B **98**, 085435 (2018).

29 M. J. Park, Y. Kim, G. Y. Cho, and S. Lee. Phys. Rev. Lett. **123**, 216803 (2019).

30 See https://support.lumerical.com/hc/en-us/articles/360041567454-Bandstructure-of-planar-photonic-crystal-with-a-hexagonal-lattice

31 E. Y. Andrei and A. H. MacDonald, Nat. Mater. **19**, 1265 (2020).

32 Y. Yang, H. Jiang, and Z. H. Hang, Sci. Rep. **8**, 1588 (2018).

33 H. A. Haus and W. Huang, W. in Proc. IEEE **79**, 10 (1991).

34 F.-J. Shu, C.-L. Zou, W.-C. Chen, and F.-W. Sun, J. Opt. Soc. Am. *B* **31**, 3 (2014).

35 P. R. Wallace, Phys. Rev. **71**, 622 (1947).

36 A. H. Castro Neto, F. Guinea, N. M. R. Peres, K. S. Novoselov, and A. K. Geim. Rev. Mod. Phys. **81**, 109 (2009).

37 D. Wong, et al. Phys. Rev. B **92**, 155409 (2015).

38 K. Hejazi, C. Liu, H. Shapourian, X. Chen, and L. Balents. Phys. Rev. B **99**, 035111 (2019).

39 H. C. Po, L. Zou, A. Vishwanath, and T. Senthil. Phys. Rev. X **8**, 031089 (2018).

40 B. L. Chittari, N. Leconte, S. Javvaji, J. Jung, Electron. Struct **1**, 1 (2018).

41 S. Carr, S. Fang, P. Jarillo-Herrero, and E. Kaxiras. Phys. Rev. B **98**, 085144 (2018).

42 M. Yankowitz, J. Jung, E. Laksono, N. Leconte, B. L. Chittari, K. Watanabe, T. Taniguchi, S. Adam, D. Graf, and C. R. Dean. Nature **557**, 404 (2018).

43 P. J. Schuck, D. P. Fromm, A. Sundaramurthy, G. S. Kino, and W. E. Moerner. Phys. Rev. Lett. **94**, 017402 (2005).

44 H. Xu, E. J. Bjerneld, M. Käll, and L. Börjesson. Phys. Rev. Lett. **83**, 4357 (1999).

45 T. F. Krauss. Nat. Photon. **2**, 8 (2008).

46 S.-P. Yu, J. A. Muniz, C.-L. Hung, and H. J. Kimble. Proc. Natl Acad. Sci. USA **116**, 26 (2019).

47 M. V. Rybin, I. I. Shishkin, K. B. Samusev, P. A. Belov, Y. S. Kivshar, R. V. Kiyan, B. N. Chichkov, and M. F. Limonov. Crystals **5**, 1 (2015).

48 W.-J. Chen, S.-J. Jiang, X.-D. Chen, B. Zhu, L. Zhou, J.-W. Dong, and C. T. Chan. Nat. Commun. **5**, 5782 (2014).

49 C. He, X. Ni, H. Ge, X.-C. Sun, Y.-B. Chen, M.-H. Lu, X.-P. Liu, and Y.-F. Chen. Nat. Phys. **12**, 1124 (2016).